

Facile Fabrication of Highly Porous 3D Sponge-Like Si@C Composites as High-Performance Anode Materials for Lithium-Ion Batteries

Chan-Woo Min^{+[a]}, Aqsa Nazir^{+[a]}, Hang T. T. Le,^[b] and Chan-Jin Park^{*[a]}

In this work, we synthesized highly porous 3D sponge-like mesoporous (MP)-Si@C composites using mass-scalable method. The optimized MP-Si@C 1 composite electrode, provided a reversible capacity of 1887 mAh g⁻¹ after 100 discharge-charge cycles with capacity retention of 83% at the rate of 0.1 C. At high C-rate the MP-Si@C 1 anode provided reversible capacity of 910 mAh g⁻¹ after 1000 cycles. The MP-Si@C 1/LCO full cell provide a discharge capacity of 1515 mAh g⁻¹ and it works well for 100 cycles. This outstanding electrochemical behavior of the

MP-Si@C 1 composite electrode was accredited to the exclusive structure of interconnected Si nanoparticles and the presence of the outer C thin layer. The carbon layer served as a shield, an effective buffer layer to house the extreme volume expansion issue of Si during continuous cycling. The excellent performance of the MP-Si@C 1 composite demonstrated its high applicability as potential anode material for next-generation LIBs.

Introduction

Nowadays, the development of affordable lithium-ion batteries (LIBs) having long cyclability, high energy and power density is crucial for fulfilling the mounting demands of large-grid energy storage systems (ESSs), electric vehicles (EVs), and portable electronics.^[1,2] Owing to its ultra-high theoretical capacity (~4200 mAh g⁻¹ for Li_{4.4}Si alloy), low lithiation voltage (<0.4 V vs. Li/Li⁺), and high natural availability, Si has emerged as an auspicious anode material for LIBs.^[3,4] In addition to the aforementioned advantages, Si presents inherent drawbacks, such as less electronic conductivity, low lithium-ion diffusion, and large volume expansion issue (approximately 300%) during alloying-dealloying with Li. These shortcomings result in low rate capability and rapid capacity decay of Si anodes during discharge-charge cycling.^[5–7]

So far, numerous approaches have been implemented to control the volume expansion–contraction of commercial LIBs featuring Si anodes and to enhance the electrochemical behavior of the silicon-based anodes in term of rate capability, high capacity, and long cyclability. Si nano-structuring into nanotubes, nanoparticles, nanorods, nanofilaments, nano-sheets, and porous interconnected nanoparticles has been predicted to boost the Li⁺ storage performance of Si based

anode materials.^[8–10] Among the designed nanostructures, the porous three-dimensional (3D) structure has been the most effective. This structure provides abundant voids and a mechanically firm framework, which are spacious enough to house the extreme volume expansion of Si anode during continuous cycling and shorten the ion and electron transport pathways, leading to improved anode kinetics.^[11] In addition, the introduction of electrically conductive carbonaceous materials, such as carbon nanotubes,^[12,13] metal organic frameworks (MOFs),^[14] and reduced graphene oxides,^[15] is an operative approach for overcoming the problems of Si anodes, viz. their poor electrical conductivity.^[16–18] MOFs and carbon coatings mitigate the volume expansion and provide channels to facilitate electrolyte wetting, electron and ion transport.^[19,20] To date, three methods have been successfully used to synthesize nanostructured Si: the chemical vapor deposition (CVD) (a vacuum deposition method), the fluid–liquid–solid growth method,^[21] and the Mg-thermal-reduction method.^[22,23] Typically, these synthesis methods require costly equipment and expensive raw materials, or only allow laboratory-scale fabrication. Thus, it is critical to form a suitable method for the mass-production of inexpensive and high-quality Si with high electrochemical performance for commercial LIB applications.

In a previous study,^[24] we used a modified Mg-thermal-reduction method to synthesize highly porous sponge-like interconnected Si nanoparticles. For the modified Mg-thermal-reduction method, we used NaCl as an inexpensive hard template for pore generation and a heat scavenger to control the rate of the redox reaction of Mg with SiO₂. The fabricated Si particles possessed a unique 3D architecture and a higher tapped density than Si nanoparticles with spherical or irregular layered structures.^[25] Accordingly, the Li storage capability and cycle life of the interconnected Si particles were increased significantly. To continue our research and further enhance the electrochemical behavior of highly porous sponge-like Si nano-

[a] C.-W. Min,^{*} Dr. A. Nazir,^{*} Prof. C.-J. Park
Department of Materials Science and Engineering
Chonnam National University
77, Yongbongro, Bukgu, Gwangju 61186, South Korea
E-mail: parkcj@jnu.ac.kr

[b] Dr. H. T. T. Le
School of Chemical Engineering
Hanoi University of Science and Technology
1 Dai Co Viet, Hai Ba Trung, Hanoi 10000, Vietnam

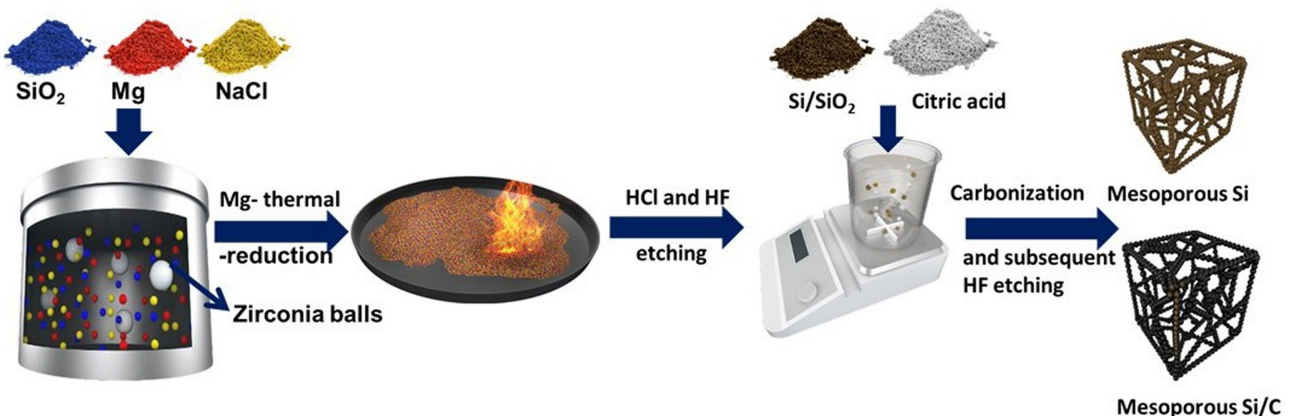
[+] These authors contributed equally to this work.

 Supporting information for this article is available on the WWW under
<https://doi.org/10.1002/batt.202100403>

particles for LIB anodes, in this study, we covered the surface of Si nanoparticles with thin carbon layers with different C contents. NaCl and citric acid were used as a pore generator and C source, respectively.^[26] After washing the by-products with ethanol water solution, porous 3D Si@C samples comprising interconnected Si nanoparticles covered with a carbon layer were obtained. The mesoporous (MP-) Si@C composite with an optimal carbon content presented an excellent electrochemical performance, a remarkable cycling stability (a reversible capacity of 1887 mAhg⁻¹ at 0.1 C rate, conforming to a retained capacity of 83% after 100 discharge–charge cycles), and superb rate capability result (476 mAhg⁻¹ at 10 C rate).

Results and Discussion

The MP–Si@C composites synthesis from nanosized SiO₂ is illustrated in Scheme 1. The crystal structure phase purity of all the samples was determined using XRD analysis. The diffraction peaks of pure MP–Si and the MP–Si@C composites were indexed assuming that Si consisted of cubic crystals (JCPDS: 27–1402) (Figure 1a).^[27] We also analyzed the XRD diffraction patterns of the MP–Si@C samples before subjecting them to HF etching and identified diffraction peaks corresponding to impurity phases, such as Mg₂S, NaCl, and MgO. The diffraction peaks of the impurity phases disappeared after HF etching,



Scheme 1. Schematic for the synthesis of M–Si/C composites.

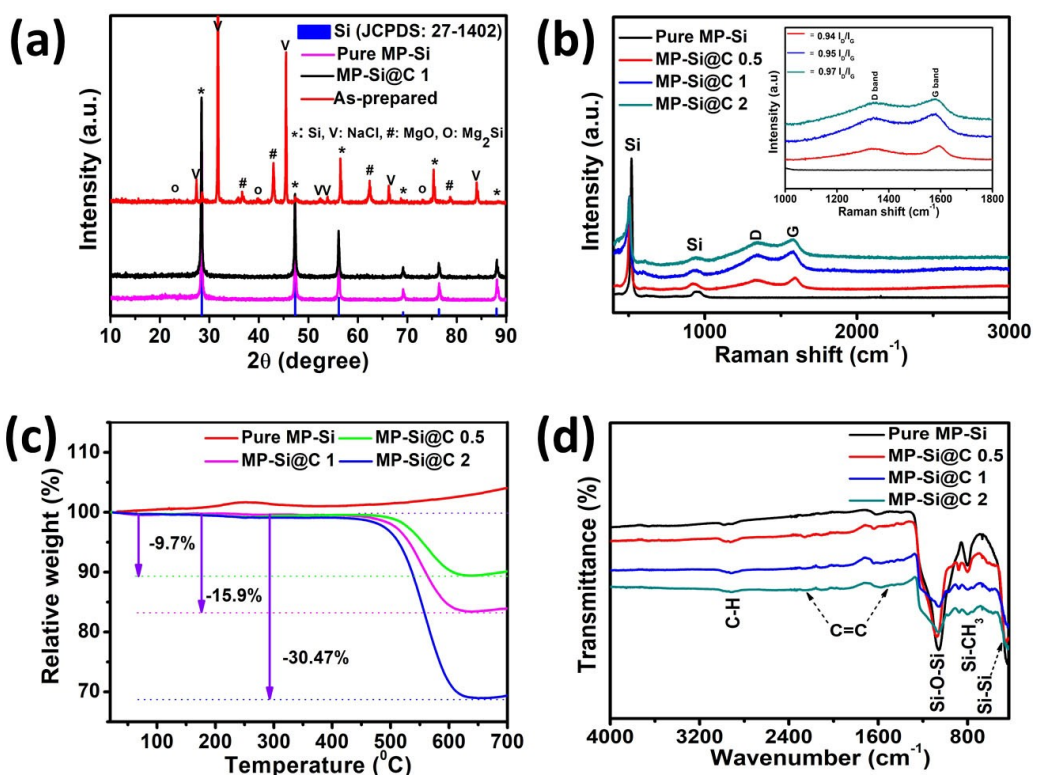


Figure 1. a) XRD patterns, b) Raman spectra, c) TGA plots in air, and d) FTIR spectra of pure MP–Si and MP–Si@C composites.

suggesting the complete removal of impurities after etching. Furthermore, the XRD patterns confirmed that the residual SiO_2 phase generated during the Mg-reduction reaction was removed, and pure, highly crystalline MP–Si was obtained. After C coating, pure MP–Si was transformed into MP–Si@C composites with different C contents depending on the amount of citric acid used as the C source. Because of the amorphous nature of the C coating, only the diffraction peaks of crystalline Si were detected in the XRD pattern of the representative MP–Si@C 1 sample.

Raman spectroscopy examination was performed to check the nature of the carbon coating of the MP–Si@C composites samples (Figure 1b).^[28] The spectra of all the MP–Si@C samples showed a sharp scattering peak at $516\text{--}524\text{ cm}^{-1}$ and a broad peak at $\sim 940\text{ cm}^{-1}$, confirming the crystallinity of Si in the fabricated composite samples.^[29] Additionally, the Raman spectra of the MP–Si@C composite samples included two dominant scattering bands at 1367 and 1569 cm^{-1} .^[30,31] The former was attributed to the D band derived from structural defects, edge effects, and dangling $\text{sp}^2\text{-C}$ bonds, and the latter was ascribed to the G band derived from the in-plane stretching of $\text{sp}^2\text{-C}$ atoms in carbonaceous materials. The inset of Figure 1(b) highlights the I_D/I_G are 0.94 , 0.95 and 0.97 for the MP–Si@C 0.5 MP–Si@C 1, and MP–Si@C 2 composite, respectively. These descriptions verified that a thin carbon layer was successfully formed on the Si nanoparticles. Furthermore, Raman spectroscopy analysis confirmed the high crystallinity of Si in the synthesised MP–Si@C composite samples.

Although C served as a buffer layer and conducting agent, it was also a less active electrode material in the MP–Si@C composites. Therefore, the C content of the composites is an important parameter that should be evaluated. The thermal stability of the composites used as LIB anode materials is another crucial factor that should be analysed. Therefore, in this study, to determine the percentage of C in the composites and to evaluate the thermal stability of the composites, TGA was performed under an air atmosphere.^[32] No weight loss was observed in the TGA profile of pure MP–Si upon increasing temperature (Figure 1c). The weight-gaining steps at 250 and 550°C in the TGA profile of pure MP–Si were attributed to the oxidation of Si in air to form SiO_2 . By contrast, all the MP–Si@C composite samples experienced weight loss because of the combustion of C upon increasing temperature. Particularly, the weight loss of the MP–Si@C composites started at 475°C , and the actual citric acid-derived carbon wt% of the MP–Si@C 0.5, MP–Si@C 1, and MP–Si@C 2 composites was estimated to be ~ 9.7 , ~ 15.9 , and ~ 30.4 wt%, correspondingly.

The Fourier-transform infrared (FTIR) spectra of all the MP–Si@C composites in the $400\text{--}4000\text{ cm}^{-1}$ wavenumber range are presented in Figure 1(d). Moreover, the characteristic absorption peaks for the vibration of the Si–Si and Si–O–Si bonds at 451 and at 1053 cm^{-1} , respectively, and the absorption bands corresponding to the vibration of the C–H, C=C, and C–C bonds were observed in the FTIR spectra of the MP–Si@C composites in the wavenumber range of $1100\text{--}2200\text{ cm}^{-1}$.^[33,34]

Furthermore, XPS measurements were used to analyze the surface chemistry of the MP–Si@C composites. The XPS profile of the representative MP–Si@C 1 composite is illustrated in Figure S1. The peaks in the XPS wide scan of the MP–Si@C 1 sample corresponded to Si 2p, Si 2s, C 1s, and O 1s (Figure S1a).

No Mg-, Na- or Cl-related peaks were present in the XPS profile of the MP–Si@C 1 composite, demonstrating the complete removal of impurity phases from the synthesised composite, as mentioned above. The Si 2p XPS profile of the MP–Si@C 1 composite was deconvoluted into three major sub-peaks at binding energies of 99.7 , 99.9 , and 104.1 eV , which were ascribed to the $\text{Si } 2\text{p}_{3/2}$ and $\text{Si } 2\text{p}_{1/2}$ peaks of Si^0 and SiO_2 , correspondingly (Figure S1b).^[35] The presence of the SiO_2 peak was attributed to the re-oxidation of Si during the washing and carbonisation steps of the synthesis process.^[36] Furthermore, the C 1s high-resolution XPS profile of the MP–Si@C 1 composite consisted of three peaks with binding energies of 284.9 , 286.4 , and 288.9 eV , which were assigned to the Si–C, C–C, and O–C=O bonds, correspondingly (Figure S1c). In addition, the O 1s XPS profile of the MP–Si@C 1 composite was deconvoluted into three main peaks at binding energies of 531.7 , 532.9 , and 533.8 eV , which were ascribed to CO_3^{2-} , SiO/SiO_2 , and C–O bonds, respectively.^[37–39]

The SEM images of all samples are illustrated in Figure 2. The pure MP–Si sample exhibited a 3D structure of interconnected Si nanoparticles and numerous pores. The pores were considered to be space voids generated after HF etching to remove the impurity phases, such as MgO , NaCl , and Mg_2Si during composite synthesis. The average size of the interconnected Si particles ranged between 20 and 30 nm and was similar to that of the initial SiO_2 precursor (Figure S2). The morphology of the composite MP–Si@C samples resembled that of pure MP–Si (Figures 2b–d). Nevertheless, the pore size of the composites was smaller than that of pure MP–Si, especially for the composites with higher C content. This was attributed to citric acid, which served as the C source, filling the available voids in the structure of pure MP–Si, followed by carbonization to generate the outer C layer. Thus, the C layer

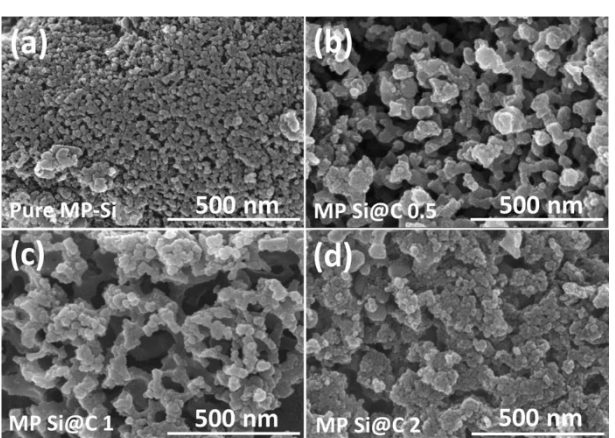


Figure 2. High-resolution SEM images of a) pure MP–Si and b) MP–Si@C 0.5, c) MP–Si@C 1, and d) MP–Si@C 2 composites.

occupied the partial void space in MP–Si and induced a decrease in pore size.

The specific surface area and pore volume of all the samples were calculated using N_2 adsorption–desorption isotherm measurements with the help of BET and Barrett–Joyner–Halenda (BJH) equations. The BET surface areas of pure MP–Si and the MP–Si@C 0.5, MP–Si@C 1, and MP–Si@C 2 composites were 82.9, 96.5, 260.7, and $273.4\text{ m}^2\text{ g}^{-1}$, respectively (Figures 3a–d). Moreover, from the BJH calculation, the mean pore sizes of pure MP–Si and the MP–Si@C 0.5, MP–Si@C 1, and MP–Si@C 2 composites were 31.7, 11.6, 10.9, and 9.7 nm, respectively.

Therefore, the surface area of the composites gradually increased with increasing C content, unlike their mean pore size. The presence of abundant pores with a size lower than 10 nm was closely associated with the increase in surface area of the composites (Figure 3, insets). In other words, after carbon was coated onto MP–Si, the pore size distribution of the MP–Si@C composites shifted towards more mesopore range. Hence, it was concluded that the fabricated composites were mesoporous materials.

To further elucidate the internal structure of the composites, a sample of the representative MP–Si@C 1 sample was subjected to TEM analysis. The porous structure of the MP–Si@C 1 sample was easily recognisable from the alternate distribution of black spots, representing Si particles, and white spots, representing pores, which were formed during HF etching of the embedded impurity phases, such as Mg_2Si , NaCl, and MgO during composite synthesis (Figure 4a). The presence

of such pores was crucial for alleviating the Si large volume expansion during alloying. Furthermore, the nanocrystalline nature of the Si particles in the MP–Si@C 1 composite was confirmed using HR-TEM (Figure 4b). The ~20 nm Si particles were interconnected because they slightly fused during the exothermic Mg-thermal-reduction step of the synthesis process. The higher-resolution TEM image of the MP–Si@C 1 composite sample in Figure 4(c) also revealed that each crystalline Si nanoparticle was thoroughly coated with a 7–10 nm thick amorphous C layer, which was derived from citric acid.^[40] The HR-TEM images allowed us to determine the *d*-spacing of the crystalline planes of the MP–Si@C 1 composite. The *d*-spacing of crystalline Si (inset of Figure 4b), which was measured to be 0.313 nm (Figure S3), corresponded to the (111) plane of Si. Furthermore, using selected area electron diffraction (SAED) pattern analysis, we confirmed the nanocrystalline nature of the MP–Si@C 1. Particularly, the rings of bright spots in the SAED pattern of the MP–Si@C 1 composite corresponded to the diffraction of the (111), (220), and (311) crystal facets of Si nanoparticles (Figure 4e).^[32] The bright-field TEM image and the energy-dispersive X-ray spectroscopy (EDS) elemental mappings of the MP–Si@C 1 composite are presented in Figures 4(f–i). The even distribution of Si and C in the MP–Si/C 1 composite confirmed that C was thoroughly covered on the Si nanoparticles surface. In addition, because Si underwent partial oxidation during the synthesis of the MP–Si@C composites and C presented unavoidable surface defects (Figure S1c), O was present in the synthesised MP–Si@C 1 composite.

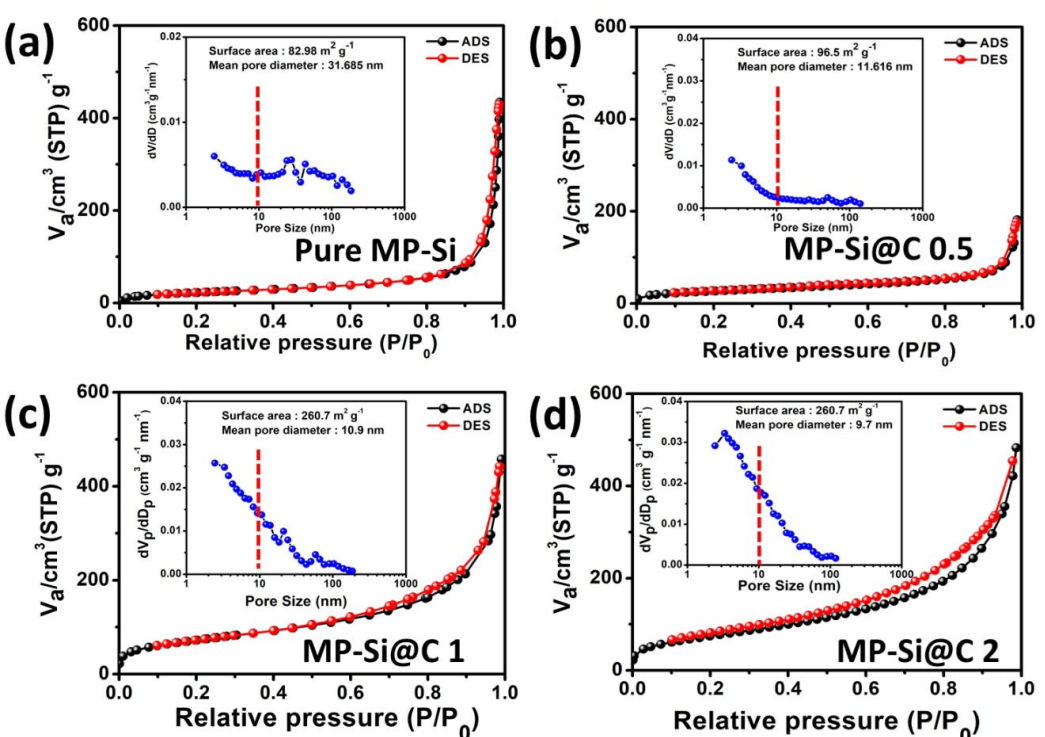


Figure 3. Nitrogen adsorption-desorption isotherms of a) pure MP–Si and b) MP–Si@C 0.5, c) MP–Si@C 1, and d) MP–Si@C 2 composites. BJH pore distribution of the corresponding in the insets.

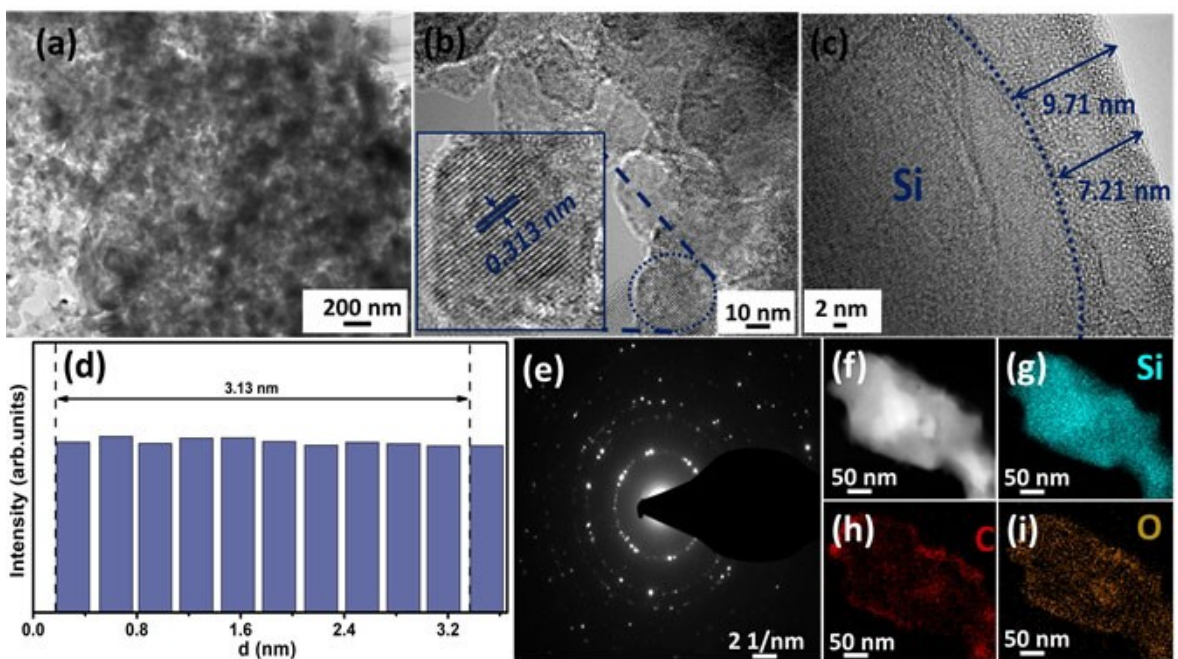


Figure 4. a) Low- and b, c) high-resolution TEM images of the MP–Si@C 1 composite. d) Corresponding d -spacings of the MP–Si@C 1 composite. e) SAED pattern of the area marked with a circle in (b). f) Bright-field STEM, and g) Si, h) C, and i) O EDS elemental mappings of the MP–Si@C 1 composite.

To study the potential application of the synthesised composites as active anode for LIBs, the MP–Si@C composites and pure MP–Si were subjected to CV testing in the 0.01–1.5 V potential range at 0.1 mV s^{-1} scanning rate. The CV graphs of

pure MP–Si and the MP–Si@C 0.5, MP–Si@C 1, and MP–Si@C 2 composites are presented in Figure 5. The CV profiles of all the samples presented almost a similar shape. In particular, the first cathodic peak of pure MP–Si (Figure 5a) emerged at a very low

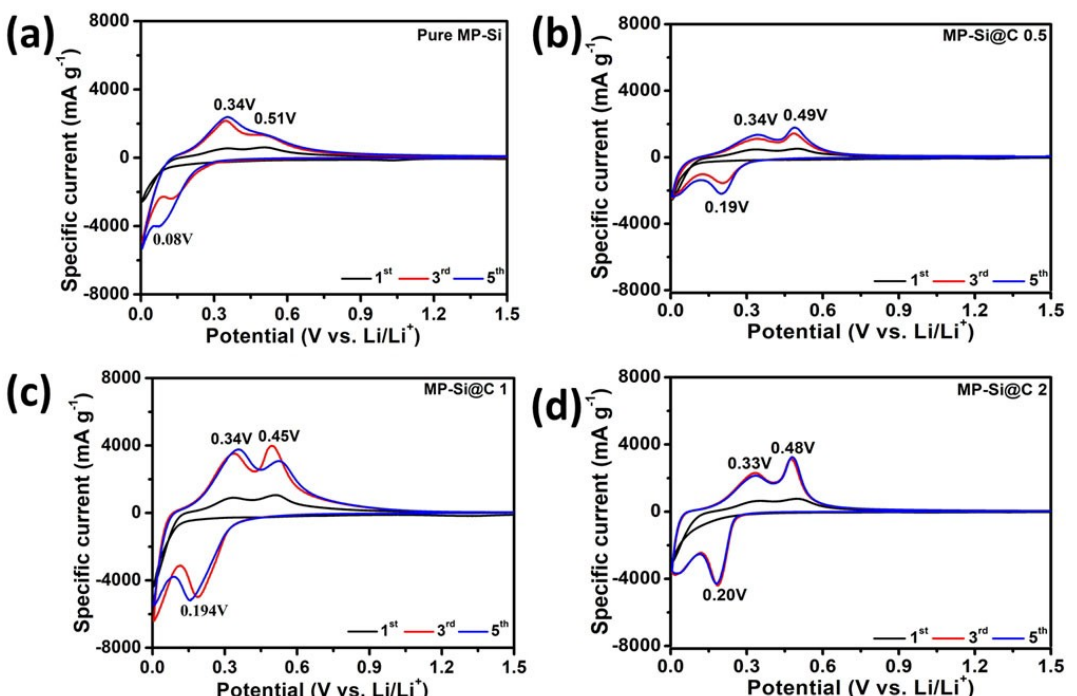


Figure 5. Cyclic voltammograms of a) pure MP–Si and b) MP–Si@C 0.5, c) MP–Si@C 1, and d) MP–Si@C 2 composites at a scan rate of 0.1 mV s^{-1} for five discharge–charge cycles.

potential of 0.013 V, conforming to the formation of Li and crystalline Si alloy. During the following anodic scan, two oxidation peaks emerged at 0.34 and 0.51 V, corresponding to the phase transitions from $\text{Li}_{15}\text{Si}_4$ to amorphous Li_xSi and from amorphous Li_xSi to amorphous Si, respectively.^[24,42] During the following scans, the cathodic peak upshifted to 0.08 V; however, the position of the anodic peaks did not change significantly. For the composite electrodes, the cathodic and anodic peaks shifted owing to the presence of the C coatings with different C content. As the C content was increased to 30.4 wt% (MP–Si@C 2 composite), the cathodic peak corresponding to the alloying of amorphous Si to Li_xSi at 0.08 V upshifted to 0.2 V.^[16,43] This shift was attributed to the charge storage mechanism of the pyrolytic C coating of the composites.^[44] The anodic and cathodic peaks of the MP–Si@C 1 composite were higher than those of other MP–Si@C composites, suggesting the superior electrochemical behavior of the MP–Si@C 1 composite.

The discharge-charge curves of all the electrodes at 0.1 C-rate are showed in Figure 6. During the first cycle, the pure MP–Si electrode delivered the discharge and charge capacities of 3195 and 2452 mAh g^{-1} , correspondingly, conforming to an initial coulombic efficiency (ICE) of 76.9% (Figure 6a). After 100 continuous cycles, the capacity retention of the electrode was 65.7% (1611 mAh g^{-1}) with respect to the first reversible capacity. For the MP–Si@C 1 electrode, the first discharge and charge capacities were 2961 and 2274 mAh g^{-1} , respectively, the ICE was 76.8% (Figure 6b), and the capacity retention after 100 discharge–charge cycles was 83%. After 100 discharge–

charge cycles, the reversible capacities of the MP–Si@C 0.5, MP–Si@C 1, and MP–Si@C 2 composite electrodes (1687, 1887, and 1722 mAh g^{-1} , respectively) were higher than that of the pure MP–Si electrode (1611 mAh g^{-1}). The significant difference in electrochemical performance between the pure MP–Si electrode and the MP–Si@C composite electrodes was mainly attributed to the low electronic conductivity of Si in the absence of a C coating and the larger charge transfer resistance (Figure S4). The charge transfer resistance of the MP–Si@C composite samples was smaller than that of pure MP–Si, facilitating electron transfer through the electrode-electrolyte interface. However, the large surface area of the MP–Si@C 2 composite with the highest C content induced more active electrolyte decomposition at the electrode-electrolyte interface, leading to the formation of a solid-electrolyte interface (SEI) layer. Consequently, the MP–Si@C 2 composite delivered a large irreversible capacity of 821 mAh g^{-1} with a low ICE of 69%. In addition, C was a less active anode material, leading to the lower reversible capacity of the MP–Si@C 2 composite. Therefore, the optimal amount of the C coating on Si allowed the MP–Si@C composite to achieve a high capacity and stable cyclability.

To evaluate the long-term cyclability of the MP–Si@C composite electrodes, the changes in the discharge-charge capacity and coulombic efficiency (CE) of the electrodes with the number of cycles over 100 cycles were recorded, and the results are presented in Figures 7a and b. During the first cycle, the CEs of pure MP–Si and MP–Si@C 2 composite were the highest (76.9%) and lowest (69%), respectively (Figure 7b). This

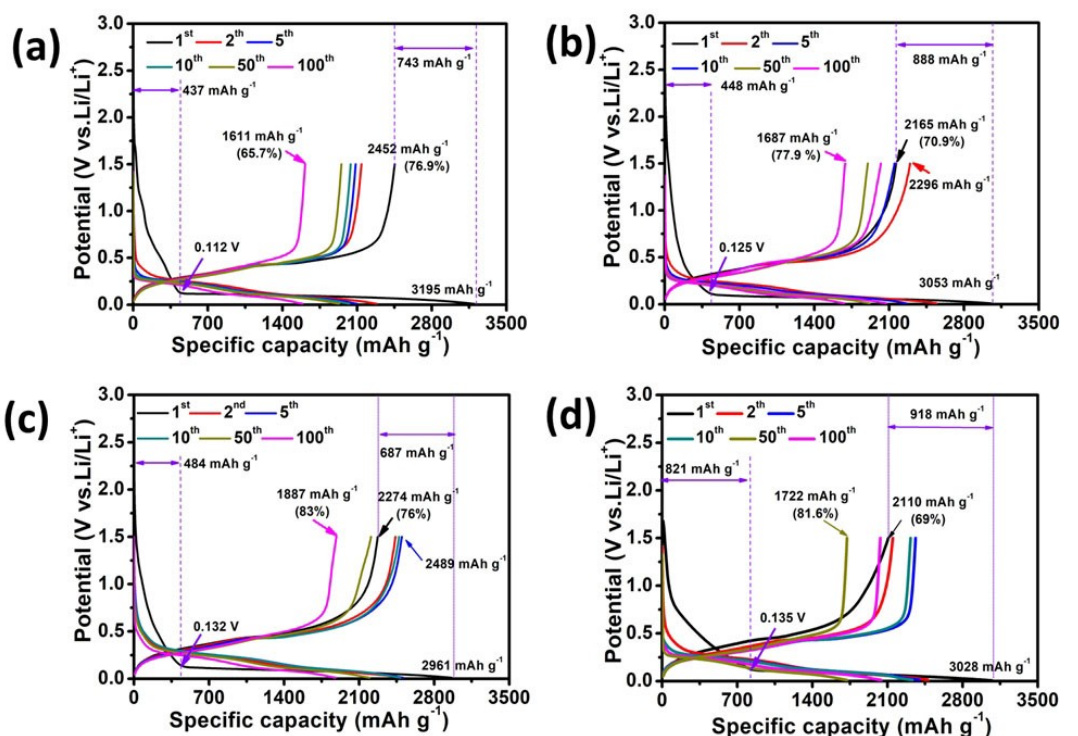


Figure 6. Galvanostatic discharge–charge potential profiles of a) pure MP–Si and b) MP–Si@C 0.5, c) MP–Si@C 1, and d) MP–Si@C 2 composites at a rate of 0.1 C for 100 cycles.

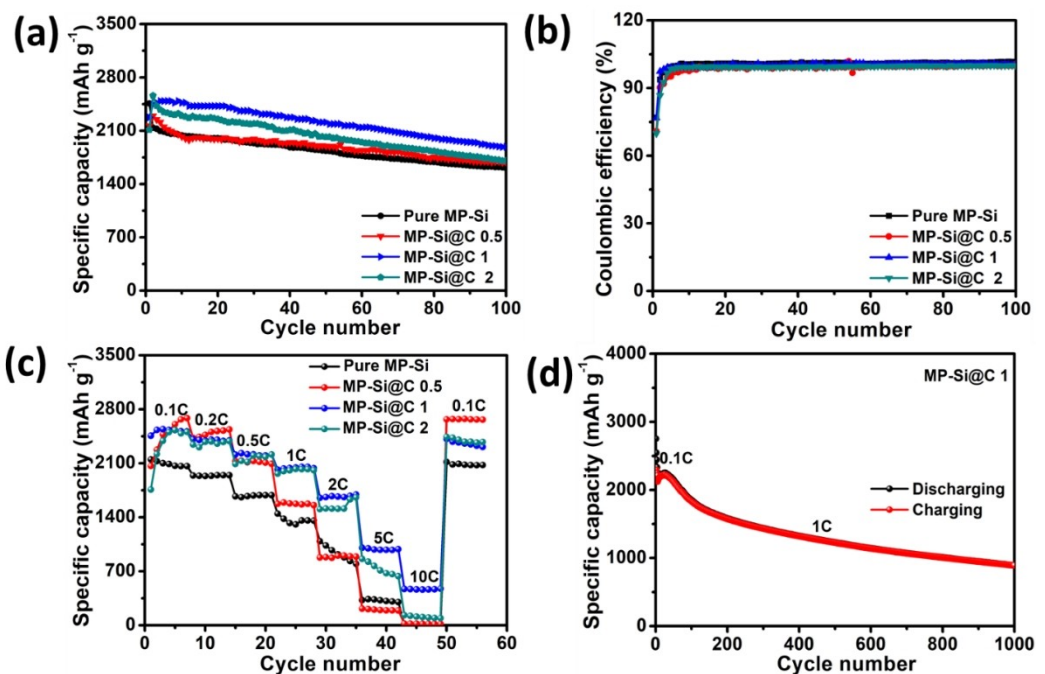


Figure 7. a) Cyclability, b) corresponding coulombic efficiency for 100 discharge–charge cycles at a rate of 0.1 C, and c) rate capability in the rate range of 0.1 C–10 C of pure MP–Si and MP–Si@C 0.5, MP–Si@C 1, and MP–Si@C 2 composites. d) Electrochemical performance of the MP–Si@C 1 composite at a rate of 1 C over 1000 discharge–charge cycles.

was attributed to the surface area of pure Si being smaller than that of the MP–Si@C composites (Figure 3) as well as the C content. Accordingly, during the first cycle, the parasitic reactions at the surface of the pure MP–Si electrode were smaller, whereas those at the surface of the MP–Si@C 2 electrode with the highest surface area and C content, were promoted. Nevertheless, from the second cycle onward, the CE of the pure MP–Si electrode increased and quickly reached a stable value of 99% after 15 cycles. The ICE of the MP–Si@C 1 composite electrode was 76%, and CE rapidly increased to 98% during the second cycle. Overall, the capacity of all the electrodes decreased during cycling. After 100 cycles, the reversible capacity (capacity retention) values of the pure MP–Si and MP–Si@C 0.5, MP–Si@C 1, and MP–Si@C 2 composite electrodes were 1611 mAh g⁻¹ (65.7%), 1687 mAh g⁻¹ (77.9%), 1887 mAh g⁻¹ (83%), and 1722 mAh g⁻¹ (81.6%), respectively (Figure 7b). Therefore, the MP–Si@C composites outperformed pure MP–Si. To elucidate the role of the carbon layer coating on the Si nanoparticles, the EIS profiles of the pure MP–Si and representative MP–Si@C 1 composite electrodes were compared. The Nyquist plots of the pure MP–Si and MP–Si@C 1 composite electrodes before cycling included an arc in the high-frequency range and a sloped line in the low-frequency range (Figure S4a). The arc represented the charge transfer resistance (R_{ct}) at the electrode–electrolyte interface and the sloped line represented the Warburg constant, which reflected the diffusion of Li⁺ ions inside the active anode materials (pure MP–Si and the MP–Si@C 1 composite). According to the data in Table S1, after equivalent circuit fitting (Figure S4b) the R_{ct} values of the uncycled pure

MP–Si and MP–Si@C 1 composite electrodes were 219 and 189 Ω, respectively. This indicated that the charge transfer of the composite electrode was facilitated by the presence of the carbon layer on the surface of Si nanoparticles.

To confirm the development of the SEI layer on the electrode surface after the first discharge–charge cycle, the EIS profiles of the pure MP–Si and MP–Si@C 1 composite electrodes were recorded after the 1st, 3rd, 5th, 10th, and 25th cycle at a specific current of 100 mAh g⁻¹. Unlike the Nyquist plots of the uncycled electrodes, those of the cycled electrodes included an additional arc in the high-to-medium-frequency region (Figure S5). This demonstrated the development of the SEI layer on the electrode surface after the first discharge–charge cycle. The presence of the SEI layer caused a rise in the interfacial resistance of the electrodes after cycling. The additional semicircles corresponding to the SEI layers appeared in high frequency region the semicircles representing R_{ct} for all the electrodes shifted to high to medium frequency regions (Figure S5a and b). Throughout the cycling test, the semicircles corresponding to the SEI layer of the MP–Si@C 1 composite electrode were much smaller than those of the pure MP–Si electrode, demonstrating the benefit of the carbon layer in inhibiting electrolyte degradation during continuous cycling.

To evaluate the electrodes microstructure integrity after cycling, the pure MP–Si and MP–Si@C 1 composite electrodes were detached from the cells after 100 cycles and subjected to SEM and TEM analysis (Figures S6 and S7). The surface morphology of the pure MP–Si and MP–Si@C 1 composite electrodes before cycling is illustrated in Figures S6(a and b), respectively, and the surface morphology of the electrodes

after 100 cycles of alloying/dealloying is presented in Figures S6(c and d), respectively. The SEM images revealed that the surface of the pure MP–Si electrode changed significantly after cycling. Numerous large cracks emerged after 100 cycles of repeated alloying/dealloying, which were accredited to the huge volume expansion of pure MP–Si in the absence of the protective C coating as a buffer layer. Consequently, the electrode pulverised, and the physical contact among Si nanoparticles, diminished. By contrast, even after 100 cycles the surface of the MP–Si@C 1 composite electrode maintained its microstructural integrity, and it is smooth and uniform. The good maintenance of the structure of MP–Si@C 1 was also revealed from the TEM image (Figure S7a). The MP–Si@C 1 composite adhered well to current collector (Cu), and slight surface decay was observed. This demonstrated the role of the conductive C coating in controlling the strain caused by repetitive alloying–dealloying of the MP–Si@C 1 composite electrode.

The rate capability and corresponding CE values of all the composite electrodes were measured for seven cycles at each C-rate, as presented in Figures 7c and S8. The reversible capacities of MP–Si@C 1 composite were 2541, 2255, 2050, 1701, 977 and 476 mAh g⁻¹ at the C-rates of 0.1 C, 0.5 C, 1 C, 2 C, 5 C, and 10 C, correspondingly. The reversible capacities of the pure MP–Si electrode at each C-rate were much smaller than those of the MP–Si@C 1 composite electrode.

Moreover, the electrochemical performance of the MP–Si@C 0.5 and MP–Si@C 2 composite electrodes was superior to that of the pure MP–Si electrode. However, the rate capability of the MP–Si@C 2 composite electrode was analogous to that of the MP–Si@C 1 composite electrode. Nevertheless, overall, at the highest discharge–charge rate in this study, the rate capability performance of the MP–Si@C 0.5 and MP–Si@C 2 composite electrodes was inferior to that of the MP–Si@C 1 composite electrode. This suggested that an insufficient or excessive C coating covering the surface of Si nanoparticles led to a deterioration in the electrochemical performance of the MP–Si@C composite electrodes used in LIBs. The CE values of the electrodes were measured every seven cycles when the C-rate was raised from 0.1 C to 10 C and switched back to the initial value of 0.1 C, and the results are illustrated in Figure S8. The results revealed that the CE of the pure MP–Si electrode was unstable, especially at a discharge–charge rate of 10 C. By contrast, the CE values of the composite electrodes were stable at all C-rates.

To further confirm the performance of the optimised electrode (MP–Si@C 1 composite) at high C-rates, the electrode was cycled at 1 C-rate (Figures 7d and S9). Prior to cycling at high C-rate, the anode was activated at 0.1 C for five cycles. At 1 C, the initial reversible capacity was 2123 mAh g⁻¹ with an initial Coulombic efficiency of 95%. It is noticeable that when the discharge–charge rate switched from 0.1 C to 1 C, a disturbance phenomenon is observed for initial few cycles. The abrupt switch from a low current to high current leads to instability in the structure of the MP–Si@C 1 composite electrode, accompanied by the electrode activation until the 30th cycle and after that capacity gradually decrease along with

cycling. Under the high rate of 1 C, the MP–Si@C 1 electrode still exhibits a reversible capacity of 910 mAh g⁻¹ with a Coulombic efficiency close to 100% after 1000 cycles, which indicates the excellent cyclability of the MP–Si@C 1 electrode (Figure 7d). Furthermore, except for the initial few cycles, the CE was almost 100% throughout the entire cycling test. Therefore, we believe that the remarkable electrochemical performance was attributed to their unique 3D porous architecture constructed by the interconnected Si nanoparticles covered with a conductive carbon coating, which served as a buffering matrix against the volume expansion of Si, increased the electronic conductivity of the composites, and facilitated the construction of a stable SEI layer.

The commercial LCO cathode XRD peaks graph and SEM image are shown in Figure S10. The 100 cycles performance of the LCO was shown in a half cell in the potential range of 3.5–4.2 V at the rate 0.1 C, as shown in Figure S11. Furthermore, before assembling the full cell, the MP–Si@C 1 anode was lithiated for 1 cycle in another half-cell at the rate of 0.1 C to eliminate the phenomenon of a low initial CE and to stabilize the SEI layer which majorly form during the first cycle. The capacity of the full cell was measured by considering the MP–Si@C 1 anode loading mass and the anode to cathode active material mass ratio was calculated by keeping their capacity ratio 0.9.

Figures 8a and b show the full cell's initial charge and discharge capacities of 1833 and 1515 mAh g⁻¹, respectively, corresponding to a CE of 83% (Figure S11) at the rate of 0.1 C. After 100 cycles, the MP–Si@C 1/LCO full cell supplied a discharge capacity of 826 mAh g⁻¹, corresponding to a capacity retention of 55%. These capacities of the full cell, at the first and 100th cycle, are lower than those of the half-cell using MP–Si@C 1 electrode at the same rate of 0.1 C. The MP–Si@C 1 anode and the LCO cathode showed considerably higher capacity retentions (Figures 7b and S10b). After 100 cycles, the LCO cathode reserved 85.6% of its initial reversible capacity, whereas the MP–Si@C 1 anode retained 83% of its initial reversible capacity. The main reason of capacity declining in the full cell is the absence of cyclable lithium. In the half-coin cells, a Li metal counter electrode was used and that is an almost infinite lithium supply source. This infinite lithium eradicated the capacity fading issue by maximizing the Li⁺ circulation between the Li metal and working electrode. The additional major reason for this capacity decay is that, after pre-lithiation step, the anode in the half-coin cell was taken apart to form the full cell in the following step. This resulted in the initially formed SEI layer to deteriorate, leading to the degeneration of the organic electrolyte of the full cell to produce a new SEI layer in place of the formerly spoiled SEI layer sites. Furthermore, the imbalance anode to cathode mass ratio should also be a major reason for this capacity decay.

The rate capability of the MP–Si@C 1/LCO full cell was inspected at numerous C-rates ranging from 0.1 C to 1 C as shown in Figure 8(c and d). Figure 8(c) displays that at the rate of 0.1 C, the full cell provided a high average specific discharge capacity of 1731 mAh g⁻¹. At other C-rates, i.e., 0.2, 0.4, 0.6, 0.8 and 1 C, the full cell could deliver average specific

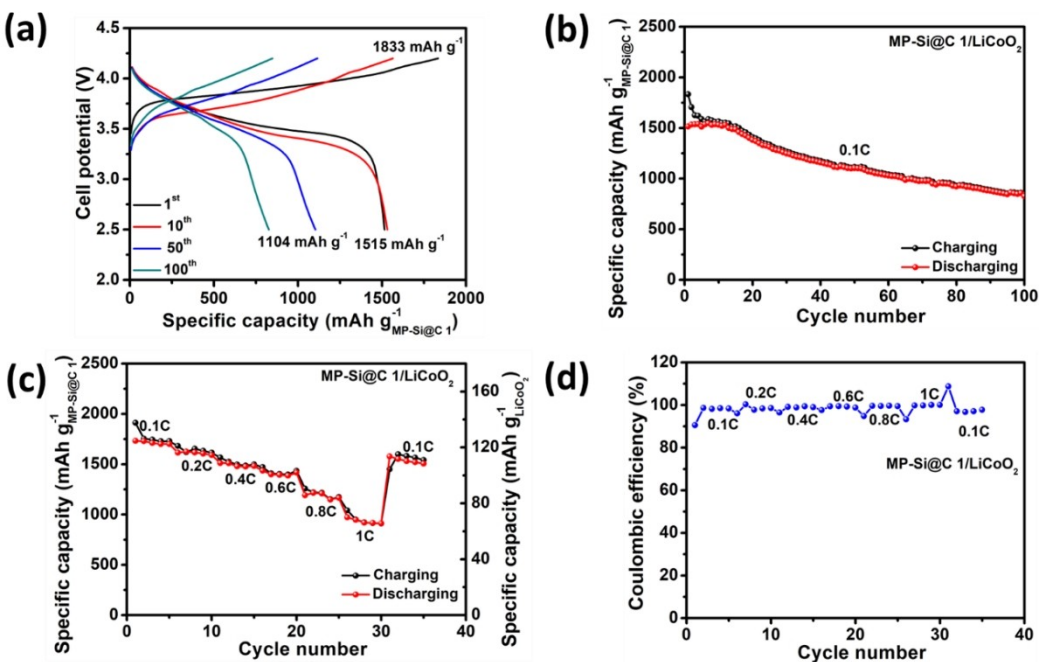


Figure 8. Electrochemical performance of a full cell composed of MP–Si@C 1 and LiCoO₂: a) Galvanostatic discharge–charge potential profiles at a rate of 0.1 C; b) cyclability up to 100 cycles; c) rate capability at different C rates; and corresponding d) Coulombic efficiency.

discharge capacities of 1615, 1511, 1436, 1192, and 972 mAh g^{-1} , correspondingly. When the C-rate switched back to the initial value of 0.1 C, the capacity observed was 1577 mAh g^{-1} , signifying the high reversibility of the MP–Si@C 1/LCO full cell. These results demonstrate that the MP–Si@C 1 composite can be efficiently used as the anode in LIBs.

Conclusions

3D mesoporous MP–Si@C composites with sponge-like structure were synthesised using a Mg-thermal-reduction method followed by convenient carbon coating. The Si nanoparticles with a particle size of ~20–30 nm was covered with a ~7–9 nm thick carbon coating. The presence of the conductive carbon coating in the composites increased electronic conductivity and promoted electrolyte wettability which subsequently enhanced Li^+ ion diffusion. Among the fabricated composites, the MP–Si@C 1 composite exhibited the best electrochemical performance. This sample delivered an initial reversible capacity of 2489 mAh g^{-1} ; moreover, after 100 discharge–charge cycles at 0.1 C-rate the reversible capacity of 1887 mAh g^{-1} was observed with a capacity retention of 83 %. In addition, the optimised sample showed extraordinary rate capability performance and delivered reversible capacities of 2541, 2255, 2050, 1701, 977 and 476 mAh g^{-1} at the C-rates of 0.1 C, 0.5 C, 1 C, 2 C, 5 C, and 10 C, correspondingly. The MP–Si@C 1/LCO full cell provide discharge capacity of 1515 mAh g^{-1} and work well for 200 cycles. Based on these results, we believe that the MP–Si@C 1 composite is a capable anode material for next-generation LIBs.

Experimental Section

Materials

NaCl (>99.8 % purity), nanosilica (>99.8 % purity), Mg metal powder (325 mesh size, >99.8 % purity, Alfa aesar), citric acid (>99.9 % purity, Alfa-aeser), hydrofluoric acid (HF, Alfa-aeser), and hydrochloric acid (HCl, Alfa-aeser) used without additional purification. Deionised (DI) water and ethanol was used as washing solvent for all the experiments in this study. Toluene (Sigma-Aldrich) was used for dissolving SbCl_3 .

Synthesis of mesoporous (MP–) Si@C composites

MP–Si@C composites were synthesised using a modified Mg-thermal-reduction method by reducing nanosized SiO_2 to Si using Mg powder. The synthesis process is illustrated in Scheme 1. First, 30 g of Mg, 30 g of SiO_2 , and 90 g of NaCl were filled to a ball-milling jar containing 10 zirconia balls. Thereafter, the ball-milling jar was rotated at 300 rpm for 3 hours. Subsequently, the precursor blend was transferred to a flat stainless-steel container, where it was set on fire using a gas torch burner in air. Under a high heat flux, the redox reaction between SiO_2 and Mg occurred rapidly and ended after a few seconds. Because of the highly exothermic reaction between SiO_2 and Mg, NaCl was added to the precursor mixture to avoid local overheating and generate a porous Si structure. After reaction completion, the impurities were removed using a 2 M HCl solution.^[25] The product obtained after etching with a dilute HF solution was washed thoroughly with a mixture of ethanol and DI water to obtain Si powder. Thereafter, the sample was vacuum dried overnight at 80 °C. Next, the fabricated Si powder was weighted and mixed with citric acid, which was used as a C source, and ethanol. MP–Si@C composites were fabricated using Si-to-citric acid mass ratios of 1:0.5, 1:1, and 1:2. After heating at 100 °C, the solid mixtures of Si and citric acid were collected and carbonised in an Ar atmosphere at 650 °C for 2 hours.

After carbonisation, the samples were etched with dilute HF to completely remove the residual SiO₂. Lastly, the samples were washed (to remove impurities) with ethanol water solution and dried out at 100 °C in vacuum. The fabricated MP–Si@C composites are named as MP–Si@C 0.5, MP–Si@C 1, and MP–Si@C 2 on the basis of citric acid to Si mass ratio used to fabricate them.

Material characterization

The phase purity and unit cell dimensions of all the samples were inspected with X-ray diffraction technique (D/MAX Ultima III, Rigaku) instrument. Raman spectra were studied using an NRS-5100 (JASCO) spectrometer (laser wavelength of 532 nm). The outer structure of the composites was assessed by using scanning electron microscopy (Hitachi, SEM; S-4700/EX-200) apparatus. The internal structure of the composites and the thickness of the C layer were characterised using a high-resolution transmission electron microscopy (HR-TEM; JEM 2100F, JEOL). The amount of carbon in the composite samples was analysed using a thermogravimetric analysis (TGA-50, Shimadzu) apparatus in an air atmosphere from 23 to 700 °C. Nitrogen adsorption–desorption isotherms were studied at –196 °C using an ASAP 2020 (Micromeritics) to get the surface area and porosimetry.

Electrochemical characterization

All the MP–Si@C composite samples were evaluated to study the electrochemical behavior using CR2032 coin cells. The anodes were made of a black slurry of MP–Si@C composite (80 wt%), super P carbon black (10 wt%), and lithium polyacrylic acid (binder) (10 wt%), in the DI water as the solvent. A doctor blade was used for casting the slurry on a Cu foil (current collector). Next, the foil was dried naturally for 1 hour and then placed for drying at 80 °C for 16 hours. Subsequently, the dried slurry was cut into 14 mm diameter disks. The electrodes loading mass was kept in 0.8–1 mg cm^{–2} range. A one molar LiPF₆ solution was prepared in dimethyl carbonate – ethylene carbonate (DMC-EC) solvent mixture with 10 wt% of fluoride ethylene carbonate (FEC) additive was used as the electrolyte for the coin cells. Li metal punched in 14 mm diameter disks and Whatman glass fiber of 18 mm diameter disks were used as the reference/counter electrode and separator, correspondingly. The half cells were prepared inside an Ar environment glovebox (O₂ concentration < 0.1 part per million (ppm) and water content < 0.1 ppm). Discharge-charge tests were performed in the 0.01–1.5 V potential range using a WBCS 3000Le32 (WonATech) battery cycler, which was also used for cyclic voltammetry (CV) analysis. Electrochemical impedance spectroscopy (EIS) was done using potentiostat with an amplitude of 10 mV in the 0.1 Hz to 100 kHz frequency range. The specific capacity of the anode materials was estimated on the active materials weight, and all measurements were done at 25 °C temperature.

Credit Authorship Contribution Statement

C.W.M.: Conceptualization, Methodology, Software, Data curation, Formal analysis. A.N.: Conceptualization, Methodology, Investigation, Formal analysis, Writing – original draft, Software, Data curation, Writing – review & editing. H.T.T.L.: Writing – review & editing . C.J.P.: Resources, Supervision, Project administration, Funding acquisition.

Acknowledgements

This study was supported by a National Research Foundation of Korea (NRF) grant funded by the MSIT, Korea (grant Nos. 2019R1A2C1084020 and 2018R1A5A1025224).

Conflict of Interest

The authors declare no conflict of interest.

Data Availability Statement

The data that support the findings of this study are available in the supplementary material of this article.

Keywords: citric acid · rate capability · reversible capacity · Si@C composite · sponge-like mesoporous material

- [1] P. Li, G. Zhao, X. Zheng, X. Xu, C. Yao, W. Sun, S. X. Dou, *Energy Storage Mater.* **2018**, *15*, 422.
- [2] L. Mathur, I.-H. Kim, A. Bhardwaj, B. Singh, J.-Y. Park, S.-J. Song, *Composites Part B* **2020**, *202*, 108405.
- [3] T. Mu, P. Zuo, S. Lou, Q. Pan, Q. Li, C. Du, Y. Gao, X. Cheng, Y. Ma, G. Yin, *Chem. Eng. J.* **2018**, *341*, 37.
- [4] J. Zhu, M. Guo, Y. Liu, X. Shi, F. Fan, M. Gu, H. Yang, *ACS Appl. Mater. Interfaces* **2019**, *11*, 17313.
- [5] P. Guan, J. Li, T. Lu, T. Guan, Z. Ma, Z. Peng, X. Zhu, L. Zhang, *ACS Appl. Mater. Interfaces* **2018**, *10*, 34283.
- [6] C. Stetson, Y. Yin, C.-S. Jiang, S. C. DeCaluwe, M. Al-Jassim, N. R. Neale, C. Ban, A. Burrell, *ACS Energy Lett.* **2019**, *4*, 2770.
- [7] Z. Y. Yang, Y. F. Yuan, M. Zhu, S. M. Yin, J. P. Cheng, S. Y. Guo, *J. Mater. Chem. A* **2021**, *9*, 22334.
- [8] W. Luo, X. Chen, Y. Xia, M. Chen, L. Wang, Q. Wang, W. Li, J. Yang, *Adv. Energy Mater.* **2017**, *7*, 1701083.
- [9] H. Liu, Y. Chen, B. Jiang, Y. Zhao, X. Guo, T. Ma, *Dalton Trans.* **2020**, *49*, 5669.
- [10] Y. Jiang, Y. Zhang, X. Yan, M. Tian, W. Xiao, H. Tang, *Chem. Eng. J.* **2017**, *330*, 1052.
- [11] G. Huang, J. Han, Z. Lu, D. Wei, H. Kashani, K. Watanabe, M. Chen, *ACS Nano* **2020**, *14*, 4374.
- [12] H. Jia, X. Li, J. Song, X. Zhang, L. Luo, Y. He, B. Li, Y. Cai, S. Hu, X. Xiao, C. Wang, K. M. Rosso, R. Yi, R. Patel, J.-G. Zhang, *Nat. Commun.* **2020**, *11*, 1474.
- [13] Y. F. Yuan, Q. Chen, M. Zhu, G. S. Cai, S. Y. Guo, *J. Alloys Compd.* **2021**, *851*, 156795.
- [14] Y. Han, P. Qi, X. Feng, S. Li, X. Fu, H. Li, Y. Chen, J. Zhou, X. Li, B. Wang, *ACS Appl. Mater. Interfaces* **2015**, *7*, 2178.
- [15] J.-G. Ren, C. Wang, Q.-H. Wu, X. Liu, Y. Yang, L. He, W. Zhang, *Nanoscale* **2014**, *6*, 3353.
- [16] A. Nazir, H. T. T. Le, C.-W. Min, A. Kasbe, J. Kim, C. soojin Jin, C.-J. Park, *Nanoscale* **2020**, *12*, 1629.
- [17] H. Wang, J. Fu, C. Wang, J. Wang, A. Yang, C. Li, Q. Sun, Y. Cui, H. Li, *Energy Environ. Sci.* **2020**, *13*, 848.
- [18] Q. Wei, G.-C. Liu, C. Zhang, X.-J. Hong, C.-L. Song, Y. Yang, M. Zhang, W. Huang, Y.-P. Cai, *Electrochim. Acta* **2019**, *317*, 583.
- [19] F. Dai, R. Yi, H. Yang, Y. Zhao, L. Luo, M. L. Gordin, H. Sohn, S. Chen, C. Wang, S. Zhang, D. Wang, *ACS Appl. Mater. Interfaces* **2019**, *11*, 13257.
- [20] Y. Q. Zheng, Y. F. Yuan, Z. W. Tong, H. Yin, S. M. Yin, S. Y. Guo, *Nanotechnology* **2020**, *31*, 215407.
- [21] C. K. Chan, R. N. Patel, M. J. O'Connell, B. A. Korgel, Y. Cui, *ACS Nano* **2010**, *4*, 1443.
- [22] Y. Zhang, K. Hu, Y. Zhou, Y. Xia, N. Yu, G. Wu, Y. Zhu, Y. Wu, H. Huang, *Nanomaterials* **2019**, *9*, 1624.

- [23] A. Ramar, F.-M. Wang, In *Nanostructured, Functional, and Flexible Materials for Energy Conversion and Storage Systems*, Elsevier, 2020, pp.465–491.
- [24] D. T. Ngo, H. T. T. Le, X.-M. Pham, J.-W. Jung, N. H. Vu, J. g. Fisher, W.-B. Im, I.-D. Kim, C.-J. Park, *J. Mater. Chem. A* **2018**, *6*, 2834.
- [25] J.-Y. Li, G. Li, J. Zhang, Y.-X. Yin, F.-S. Yue, Q. Xu, Y.-G. Guo, *ACS Appl. Mater. Interfaces* **2019**, *11*, 4057.
- [26] Y. Chen, J. Zhang, X. Chen, P. Yang, M. An, *Ceram. Int.* **2019**, *45*, 17040.
- [27] M. Azadeh, C. Zamani, A. Ataie, J. R. Morante, *Mater. Today Commun.* **2018**, *14*, 141.
- [28] C. Shen, X. Fang, M. Ge, A. Zhang, Y. Liu, Y. Ma, M. Mecklenburg, X. Nie, C. Zhou, *ACS Nano* **2018**, *12*, 6280.
- [29] Z. Yi, N. Lin, T. Xu, Y. Qian, *Chem. Eng. J.* **2018**, *347*, 214.
- [30] H. Okuda, R. J. Young, D. Wolverson, F. Tanaka, G. Yamamoto, T. Okabe, *Carbon* **2018**, *130*, 178.
- [31] A. Nazir, H. T. T. Le, A.-G. Nguyen, C.-J. Park, *Electrochim. Acta* **2021**, *138750*.
- [32] C. Jo, A. S. Groombridge, J. De La Verpilliere, J. T. Lee, Y. Son, H.-L. Liang, A. M. Boies, M. De Volder, *ACS Nano* **2020**, *14*, 698.
- [33] R. Toivola, F. Afkhami, S. Baker, J. McClure, B. D. Flinn, *Polym. Test.* **2018**, *69*, 490.
- [34] P. Li, G. Chen, Y. Lin, F. Chen, L. Chen, N. Zhang, Y. Cao, R. Ma, X. Liu, *Macromol. Chem. Phys.* **2020**, *221*, 1900414.
- [35] J. Li, Z. Li, W. Huang, L. Chen, F. Lv, M. Zou, F. Qian, Z. Huang, J. Lu, Y. Li, *Small* **2019**, *15*, 1900436.
- [36] J. Xie, B. Li, H. Peng, Y. Song, J. Li, Z. Zhang, Q. Zhang, *Angew. Chem. Int. Ed.* **2019**, *58*, 4963.
- [37] A. Bhardwaj, I.-H. Kim, L. Mathur, J.-Y. Park, S.-J. Song, *J. Hazard. Mater.* **2021**, *403*, 123797.
- [38] J. Gao, Y. Wang, H. Wu, X. Liu, L. Wang, Q. Yu, A. Li, H. Wang, C. Song, Z. Gao, M. Peng, M. Zhang, N. Ma, J. Wang, W. Zhou, G. Wang, Z. Yin, D. Ma, *Angew. Chem. Int. Ed.* **2019**, *58*, 15089.
- [39] W. Beichel, J. Skrotzki, P. Klose, C. Njel, B. Butschke, S. Burger, L. Liu, R. Thomann, Y. Thomann, D. Biro, S. Thiele, I. Krossing, *Batteries & Supercaps* **2021**, batt.202100347.
- [40] B. Wang, Z. Zhang, K. Chang, J. Cui, A. Rosenkranz, J. Yu, C.-T. Lin, G. Chen, K. Zang, J. Luo, N. Jiang, D. Guo, *Nano Lett.* **2018**, *18*, 4611.
- [41] Y. Zhang, K. Hu, J. Ren, Y. Wu, N. Yu, A. Feng, Z. Huang, Z. Jia, G. Wu, *Dalton Trans.* **2019**, *48*, 17683.
- [42] A. Nazir, H. T. T. Le, A. Kasbe, C.-J. Park, *Chem. Eng. J.* **2021**, *405*, 126963.
- [43] B. Wang, W. Li, T. Wu, J. Guo, Z. Wen, *Energy Storage Mater.* **2018**, *15*, 139.
- [44] H. T. T. Le, T.-D. Dang, N. T. H. Chu, C.-J. Park, *Electrochim. Acta* **2019**, *135399*.

Manuscript received: December 20, 2021

Revised manuscript received: January 21, 2022

Accepted manuscript online: January 28, 2022

Version of record online: February 18, 2022